

# Exchange of molecular and cellular information: a hybrid model that integrates stem cell divisions and key regulatory interactions

Lisa Van den Broeck<sup>1</sup>, Ryan J. Spurney<sup>2</sup>, Adam P. Fisher<sup>1</sup>, Michael Schwartz<sup>1</sup>, Natalie M. Clark<sup>3</sup>, Thomas T. Nguyen<sup>1</sup>, Imani Madison<sup>1</sup>, Mariah Gobble<sup>1</sup>, Terri Long<sup>1</sup>, Rosangela Sozzani<sup>1\*</sup>

<sup>1</sup>Plant and Microbial Biology Department, North Carolina State University, Raleigh, NC 27695

<sup>2</sup>Electrical and Computer Engineering Department, North Carolina State University, Raleigh, NC 27695

<sup>3</sup>Department of Plant Pathology and Microbiology, Iowa State University, Ames, Iowa 50010

\*Corresponding author: [ross\\_sozzani@ncsu.edu](mailto:ross_sozzani@ncsu.edu)

ORCIDs:

Lisa Van den Broeck (0000-0003-0226-0757)

Natalie M. Clark (0000-0003-0988-321X)

Rosangela Sozzani (0000-0003-3316-2367)

Terri Long (0000-0001-7846-0195)

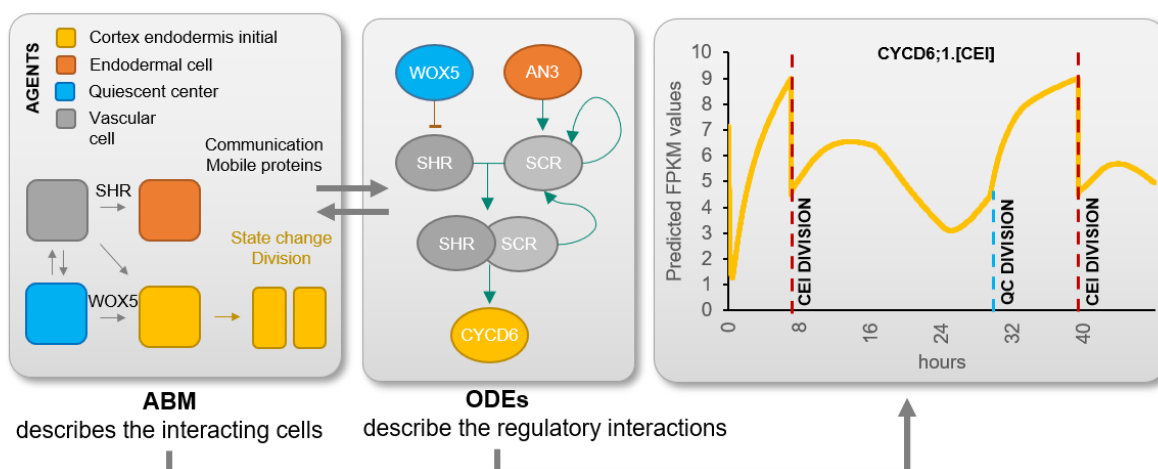
Michael Schwartz (0000-0002-5434-6248)

Ryan Spurney (0000-0001-9915-3370)

## Abstract

Stem cells give rise to the entirety of cells within an organ. Maintaining stem cell identity and coordinately regulating stem cell divisions is crucial for proper development. In plants, mobile proteins, such as WOX5 and SHR, regulate divisions in the root stem cell niche (SCN). However, how these proteins coordinately function to establish systemic behavior is not well understood. We propose a non-cell autonomous role for WOX5 in the CEI and identify a regulator, AN3/GIF1, that coordinates CEI divisions. Here we show with a multiscale hybrid model integrating ODEs and agent-based modeling that QC and CEI divisions have different dynamics. Specifically, by combining continuous models to describe regulatory networks and agent-based rules, we model systemic behavior, which led us to predict cell-type-specific expression dynamics of SHR, SCR, WOX5, AN3, and CYCD6;1, and experimentally validate CEI cell divisions. Conclusively, our results show an interdependency between CEI and QC divisions.

## Thumbnail image



## Keywords

Root stem cell niche, AN3, WOX5, cortex endodermal initial divisions, agent-based modeling, ordinary differential equations, hybrid multiscale modeling

1 **Introduction**

2 Stem cells divide to regenerate themselves and to generate all of the cell- and tissue-types in a  
3 multicellular organism, such as plants. The continued ability to sustain stem cells within their micro-  
4 environment, the stem cell niche (SCN), is an important developmental characteristic that ensures  
5 proper tissue growth. The *Arabidopsis thaliana* root SCN contains four stem cell populations, the  
6 columella stem cells (CSCs), the cortex endodermis initial (CEI) cells, the vascular initial cells, and the  
7 epidermal/lateral root cap initials, which form the entire root as a result of consecutive cell divisions  
8 (Dinneny & Benfey, 2008; Fisher & Sozzani, 2016). The different populations of stem cells are  
9 maintained by the quiescent center (QC) through the generation of short-range signals that repress  
10 cell differentiation (Clark, Fisher, et al., 2020; Pi et al., 2015; van den Berg et al., 1997). A known QC-  
11 derived signal is the homeobox transcription factor (TF) WUSCHEL-RELATED HOMEOBOX 5 (WOX5),  
12 which is specifically expressed in the QC and represses the differentiation of the CSCs (Petricka et al.,  
13 2012; Sarkar et al., 2007). Specifically, non-cell-autonomous WOX5 maintenance of CSCs takes place  
14 through the repression of the differentiation factor CYCLING DOF FACTOR 4 (CDF4) (Pi et al., 2015).  
15 *wox5-1* mutants have increased QC divisions in roots and a decreased number of columella cell layers  
16 (Forzani et al., 2014). In the QC cells, WOX5 controls divisions by restricting *CYCD3;3* expression  
17 (Forzani et al., 2014). Although the regulatory modules within the CSCs and QC are well characterized  
18 (Forzani et al., 2014; Stahl et al., 2013), the molecular mechanisms by which WOX5 promotes stem cell  
19 fate of CEIs remains unknown.

20 Several proteins have been shown to positively regulate *WOX5*, such as ANGUSTIFOLIA (AN3) / GRF-  
21 INTERACTING FACTOR 1 (GIF1). AN3 is expressed in the root meristem with a high peak in expression  
22 in the SCN and QC and plays a role in maintaining QC identity (Ercoli et al., 2018). However, whether  
23 AN3 function is dependent on WOX5 and whether AN3 has a regulatory role outside the QC in the SCN  
24 is not understood. Additionally, AN3 was shown to regulate the expression of SCARECROW (SCR) (Ercoli  
25 et al., 2018), which along with SHORT-ROOT (SHR) regulates the expression of the D-type Cyclin  
26 *CYCLIND6;1* (*CYCD6;1*) to control the CEI divisions to generate the cortical and endodermal tissue layers  
27 (Cruz-Ramírez et al., 2012; Gallagher & Benfey, 2009; Long et al., 2015; Nakajima et al., 2001; Sozzani  
28 et al., 2010). Specifically, SHR moves from the vasculature to the CEI, where it forms a complex with  
29 SCR to transcriptionally regulate *CYCD6;1*.

30 The regulatory interactions between the different cell types of the root SCN are complex and non-  
31 intuitive and computational tools are essential to understanding systemic behavior. Developmental  
32 processes such as auxin flow within the root and lateral shoot branching have been mathematically  
33 modeled to better understand and predict system-level behavior (Canher et al., 2020; Prusinkiewicz et  
34 al., 2009). Some models implement different scales of the system to simulate, understand, and predict

35 system-level behavior as a whole. For example, a mathematical model that simulates and predicts the  
36 induction of shoot branching during plant development included on a molecular scale auxin flux across  
37 metamers (i.e. smaller segments of the stem) and on an organ scale the formation of metamers of the  
38 stem and lateral branches (Prusinkiewicz et al., 2009). Modeling systems and allowing exchange of  
39 information across different scales can also be achieved by combining agent-based models (ABM) with  
40 continuous models, such as ordinary differential equations (ODEs) or partial differential equations  
41 (Cilfone et al., 2015). ABMs consist of autonomous “agents” that dynamically interact and show  
42 responsive behavior through a set of simple rules. ABMs have, for example, been used to simulate  
43 plant-herbivore interactions (Radny & Meyer, 2018). However, within the molecular plant biology field,  
44 these models are not widely used, despite their capacity to capture system-level behavior. On the  
45 other hand, continuous models such as ODEs have been applied to infer gene regulatory networks  
46 (Krouk et al., 2010; Yao et al., 2011) and predict dynamic gene expression patterns (Clark, Fisher, et al.,  
47 2020). These models are computationally intensive and lack the capability to capture system-level  
48 behavior but can model complex dynamic responses over time. Hybrid models are created when, for  
49 example, continuous models are used within a discrete ABM to describe a part of the system. These  
50 hybrid models are usually multiscale models, given that the continuous models often describe a  
51 dynamical response on a different spatiotemporal scale than the ABM (Cilfone et al., 2015).

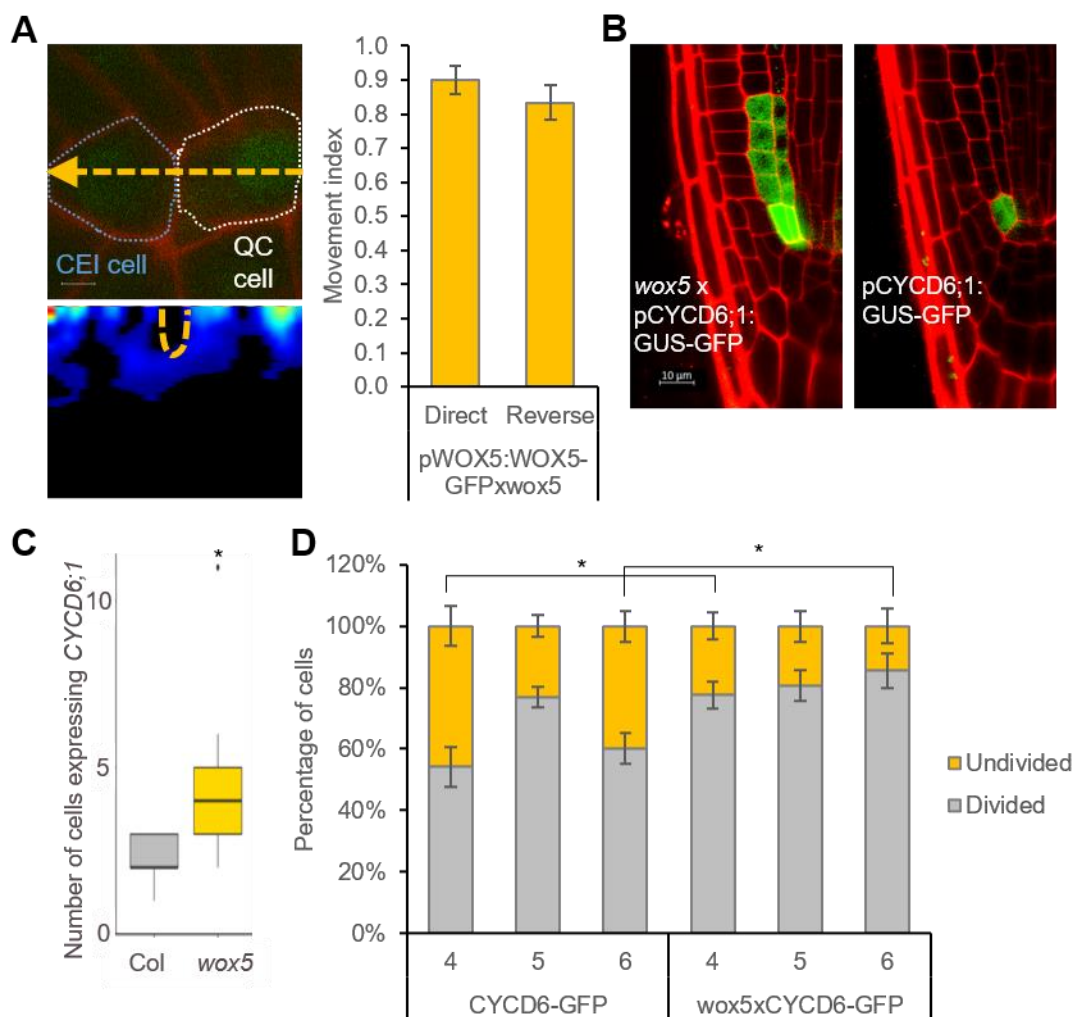
52 In this study, we combine cell-type-specific gene expression data and experimental data with network  
53 inference and parametric models to better understand how WOX5, AN3, SCR, and SHR coordinately  
54 regulate CEI stem cell divisions. We transcriptionally profiled CEI cells in wild-type and *wox5-1* roots,  
55 as well as QC cells and non-stem cells. We found that AN3 was among the most CEI-enriched genes.  
56 Additionally, the loss-of-function of *wox5* or *an3* resulted in an extended expression pattern of the CEI  
57 stem cell marker *CYCD6;1* into the cortex and endodermal cells. We built an ODE and agent-based  
58 hybrid model linking cell behavior, specifically cell division, to gene expression dynamics represented  
59 by ODEs of WOX5, AN3, SCR, SHR and CYCD6;1. Our hybrid model allowed for the exchange of  
60 information between a cellular scale (i.e. division of stem cells) and a molecular scale (i.e. regulatory  
61 interactions at single cell level). In the hybrid model, the mobile proteins, WOX5 and SHR, regulated  
62 the expression of downstream proteins non-cell autonomously in specific cell-types. The  
63 communication between cell types and dynamic expression patterns modeled experimentally  
64 validated temporal stem cell divisions.

65 **Results**

66 **WOX5 regulates CEI-specific genes**

67 The functional role of WOX5 in the QC and CSC has been extensively reported while its role in stem  
68 cell populations remains largely unknown. *WOX5* is specifically expressed in the QC cells, however, the  
69 protein moves to the CSCs and the vasculature initials and has been shown to have a non-cell  
70 autonomous role in these cells (Clark et al., 2019; Pi et al., 2015). To determine whether WOX5 is also  
71 able to move from the QC cells to the QC-neighboring CEI cells and regulate downstream targets, we  
72 used scanning fluorescence correlation spectroscopy (scanning FCS). Five-day-old  
73 *wox5xpWOX5:WOX5-GFP* plants were analyzed with scanning FCS to evaluate the directional  
74 movement of WOX5 protein between these two cell-types. Line scans were taken over time from a  
75 region spanning the CEI and adjacent QC (Fig 1A). This analysis resulted in a quantitative assessment  
76 of movement and allowed us to calculate the movement index (MI). We found that WOX5 moved  
77 bidirectionally between the QC and the CEI (MI = 0.90 ± 0.04 from QC to CEI, MI = 0.83 ± 0.05 from CEI  
78 to QC, n = 20) (Supplemental Table 1). As a comparison, within the SCN, free GFP and immobile 3xGFP  
79 have a moving index of ~0.7 and ~0.25, respectively (Clark et al., 2016).

80 To explore the potential functional role of WOX5 in CEI, we examined the expression pattern of the  
81 CEI-marker pCYCD6;1:GFP in *wox5*. The marker showed an expression pattern that extended into the  
82 cortex and endodermal cells (Fig 1B,C). This expanded expression of CYCD6;1 suggests that the 4 to 5  
83 cells proximal of the CEI, referred hereafter as CEI-like cells, have gained stem cell-like characteristics  
84 and also indicates that WOX5 controls CYCD6;1 expression to the CEI (Fig 1B). We then explored the  
85 role of WOX5 in limiting CYCD6;1 expression and, thus, controlling CEI divisions. To this end, we  
86 quantified the number of undivided and divided CEI cells in 4-, 5-, and 6-day-old *wox5* and wild-type  
87 roots. This quantification showed that *wox5xpCYCD6;1:GUS-GFP* roots had an increase of 23.43% and  
88 25.33% (p = 0.0495, Wilcoxon test) divided CEI cells compared to the wild type (WT) at 4 and 6 days,  
89 respectively (Fig 1D). Taken together, these results support a functional non-cell autonomous role for  
90 WOX5 in the CEI.



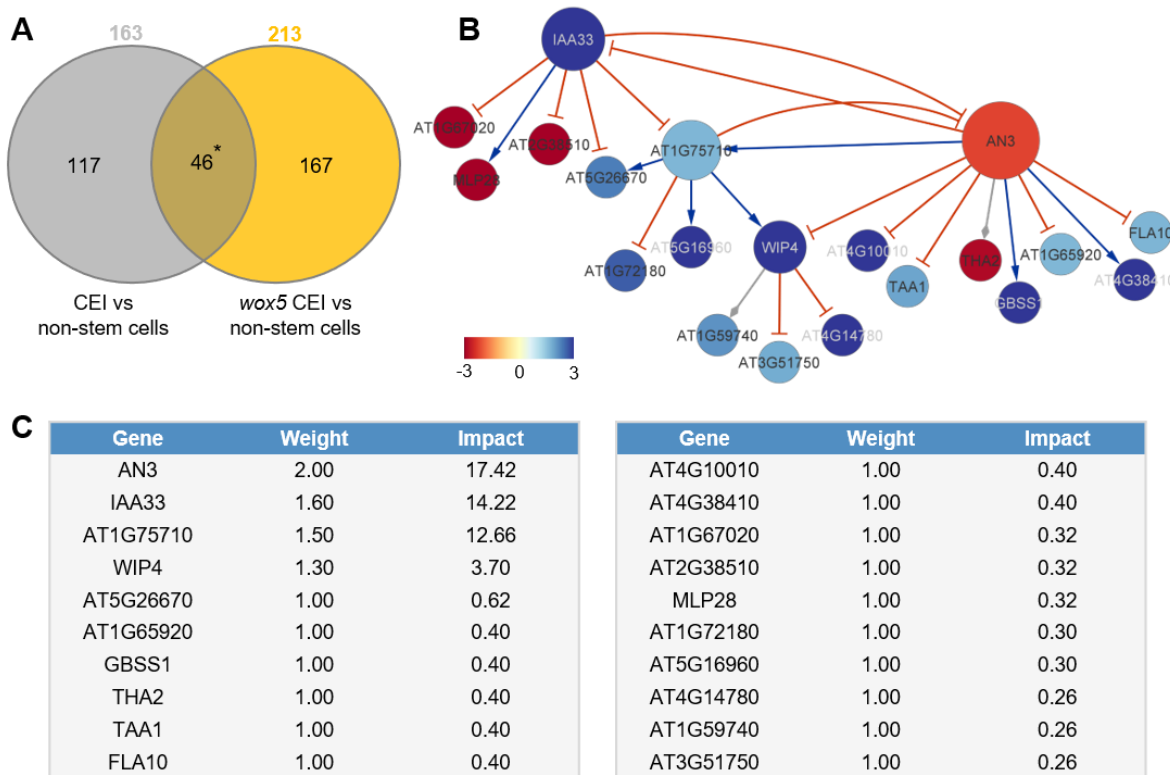
91  
92 Figure 1 – Characterization of WOX5 in the CEI. (A) (Top - left) Confocal image of a region in the *wox5xpWOX5:WOX5-GFP*  
93 root spanning the quiescent center (QC) and cortex endodermis initial (CEI) used for pCF. The location and direction of the  
94 line scan (orange dashed line) is marked onto the image. (Bottom - left) pCF carpet image of the top image. Orange, dashed  
95 regions represent an arch in the pCF carpet, which indicates movement. (Right) Movement index of *wox5xpWOX5:WOX5-*  
96 *GFP* between the QC and CEI. (B) Confocal image *wox5xpCYCD6;1:GUS-GFP* roots. (C) The number of CEI and CEI-like cells  
97 expressing *pCYCD6;1:GUS-GFP*. (D) Percentage of divided and undivided CEI cells in *pCYCD6;1:GUS-GFP* and  
98 *wox5xpCYCD6;1:GUS-GFP* roots. Data are presented as mean  $\pm$  SEM. \* =  $p < 0.05$  (C,D: Wilcoxon Chi-square test). Error bars  
99 represent SEM.

100 **Network inference and node importance analysis to identify functional candidates**

101 To unravel the transcriptional events regulating the extended expression pattern of *CYCD6;1* in the  
102 *wox5* mutant background, a transcriptome analysis was performed on FACS-sorted GFP positive cells  
103 from *pCYCD6;1:GUS-GFP*, *wox5xpCYCD6;1:GUS-GFP*, and *pWOX5:GFP*, and the meristematic cells from  
104 *pWOX5-GFP* that do not express the marker (referred to as non-stem cells) (Supplemental Table 2).  
105 Compared to the cells not expressing the *pWOX5-GFP* marker, 163 genes were differentially expressed  
106 (FDR < 0.05) in wild-type CEI cells and 213 genes in the CEI and CEI-like cells from the *wox5* mutant. In  
107 total, the union of these two analyses identified 330 DEGs in CEI and CEI-like cells, of which 159 DEGs

108 (48.18%) have previously been shown to be expressed in the SCN and 53 genes were enriched in the  
109 CEI (Clark et al., 2019). We hypothesized that the regulatory genes underlying *CYCD6;1* expression  
110 should be differentially expressed in the CEI cells (*CYCD6;1* expressing cells) of the wild-type and *wox5*  
111 roots and thus focused on the genes overlapping between these two sets of DEGs (Fig 2A). In total, 46  
112 genes overlapped between the CEI and CEI-like cells, which equals an enrichment of 35.8 ( $p < 4.431e-59$ ,  
113 Exact hypergeometric probability). To identify key regulatory proteins among these 46 genes, we  
114 predicted causal relations between the TFs and downstream genes with high accuracy and constructed  
115 a gene regulatory network. We inferred the causal relations by leveraging our transcriptome data with  
116 a regression tree algorithm RTP-STAR (Fig 2B) (Huynh-Thu et al., 2010; Spurrey et al., 2020; Van den  
117 Broeck et al., 2020). The inferred network contained 20 nodes, of which four are TFs (Fig 2B). These  
118 four TFs are: WIP DOMAIN PROTEIN 4 (WIP4), which is shown to be important for root initiation,  
119 INDOLE-3-ACETIC ACID INDUCIBLE 33 (IAA33), ANGUSTIFOLIA (AN3) / GRF-INTERACTING FACTOR 1  
120 (GIF1), which is a known regulator of cell proliferation, and an unknown TF (AT1G75710). Among the  
121 inferred AN3 targets, we confirmed with TChAP data that three targets (AT1G75710, *FLA10*, and  
122 *GBSS1*) were directly bound by AN3 (Vercruyssen et al., 2014). Network inference allowed us to identify  
123 potential functionally important genes, however, we still needed to pinpoint the biological important  
124 genes within the network.

125 To identify which genes could cause the largest impact on network stability when perturbed, we  
126 performed a node importance analysis. To calculate the impact of each gene, each node received a  
127 weight depending on its outdegree (i.e. number of outgoing edges), then for each node, the sum of  
128 the weighted outgoing first neighbors and the sum of the weighted incoming first neighbors was taken.  
129 Both sums were in turn weighted, specifically, the sum of the outgoing neighbors was weighted by  
130 Average Shortest Path Length (ASPL), and the sum of the incoming neighbors was weighted according  
131 to the proportion of end-nodes within the network, which is in this network 20% (see Materials and  
132 Methods). We next developed an R-based Shiny application (Node Analyzer) that calculates the  
133 weights and impacts of each gene within a network (Shannon et al., 2003) (see Materials and Methods)  
134 (Supplemental Fig 1). Node Analyzer allowed us to rank the 20 genes in the network and select key  
135 genes. The most impactful gene within our network is *AN3*, a transcriptional coactivator that is  
136 involved in cell proliferation during leaf and flower development (Fig 2C).



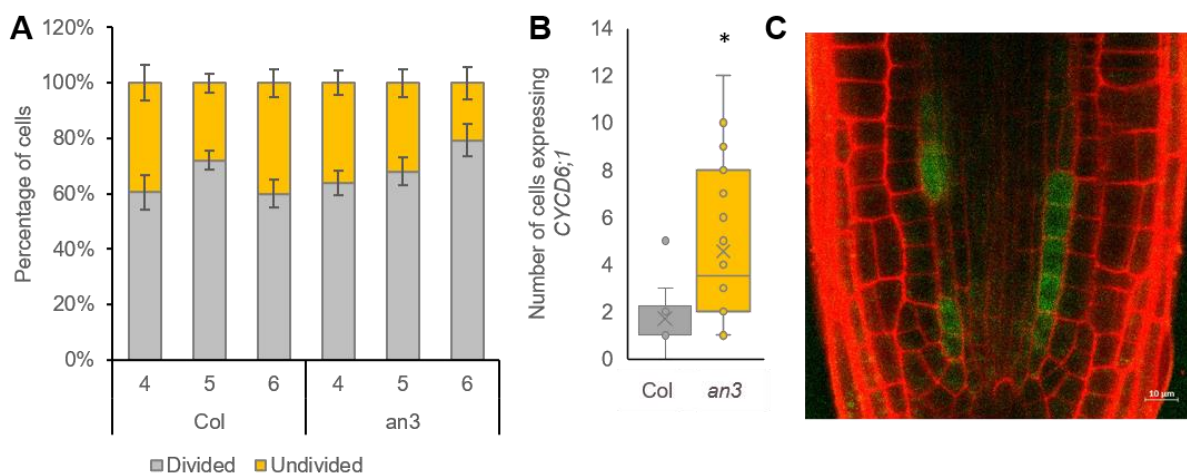
137

138 Figure 2 – Network analysis of CEI-expressed genes. (A) The overlap between genes differentially expressed between CEI cells  
 139 and non-stem cells in the wild-type and the *wox5* background. \* =  $p < 0.001$  (Exact hypergeometric probability). (B) Causal  
 140 interactions between 46 DEGs that are enriched in the CEI cells. Green arrows and red T-arrows represent activating and  
 141 repressing regulations, respectively. The size of the nodes correlates with the outdegree of that node. The color of the nodes  
 142 corresponds to the  $\log_2$  fold change in expression in the *wox5* CEI cells compared to the non-stem cells. (C) Tabular output  
 143 from the Node Analyzer application presenting the weight (calculated based on outdegree) and impact (see Materials and  
 144 Methods) of each gene.

#### 145 AN3 contributes to the regulation of CEI divisions

146 It was previously shown that *AN3/GIF1* and its closest homologs, *GIF2* and *GIF3*, were expressed in the  
 147 root stem cell niche (Ercoli et al., 2018). A triple mutant (*gif1/2/3*) displayed a disorganized QC and  
 148 increased root length as a result of an increased root meristem size (Ercoli et al., 2018). We confirmed  
 149 the growth repressing role of AN3 in the roots, as *an3* and 35S:AN3-GFP roots showed an increased  
 150 and reduced root length compared to the WT, respectively (Supplemental Fig 2A). We observed a  
 151 disorganized stem cell niche in 56% (25/45 roots) of *an3* mutant roots (Supplemental Fig 2B).  
 152 Additionally, *an3* mutants contained starch granules in the cells that are normally CSC, suggesting that  
 153 AN3 plays a role in CSC maintenance (Supplemental Fig 2C). To determine whether AN3 also plays a  
 154 role in CEI divisions, we quantified the number of undivided and divided CEI cells in 4-, 5-, and 6-day-  
 155 old *an3* and WT roots. 6-day-old *an3* roots had 19.22% fewer undivided CEI cells at compared to WT  
 156 ( $p = 0.103$ , Wilcoxon test), suggesting that more CEI divisions occur in the *an3* mutant (Fig 3A).  
 157 Additionally, when *an3* is crossed with the CEI-marker pCYCD6;1:GUS-GFP, an extended expression

158 pattern is observed (Fig 3B,C). Taken together, these results support a role for AN3 in the regulation  
159 of CEI divisions.



160

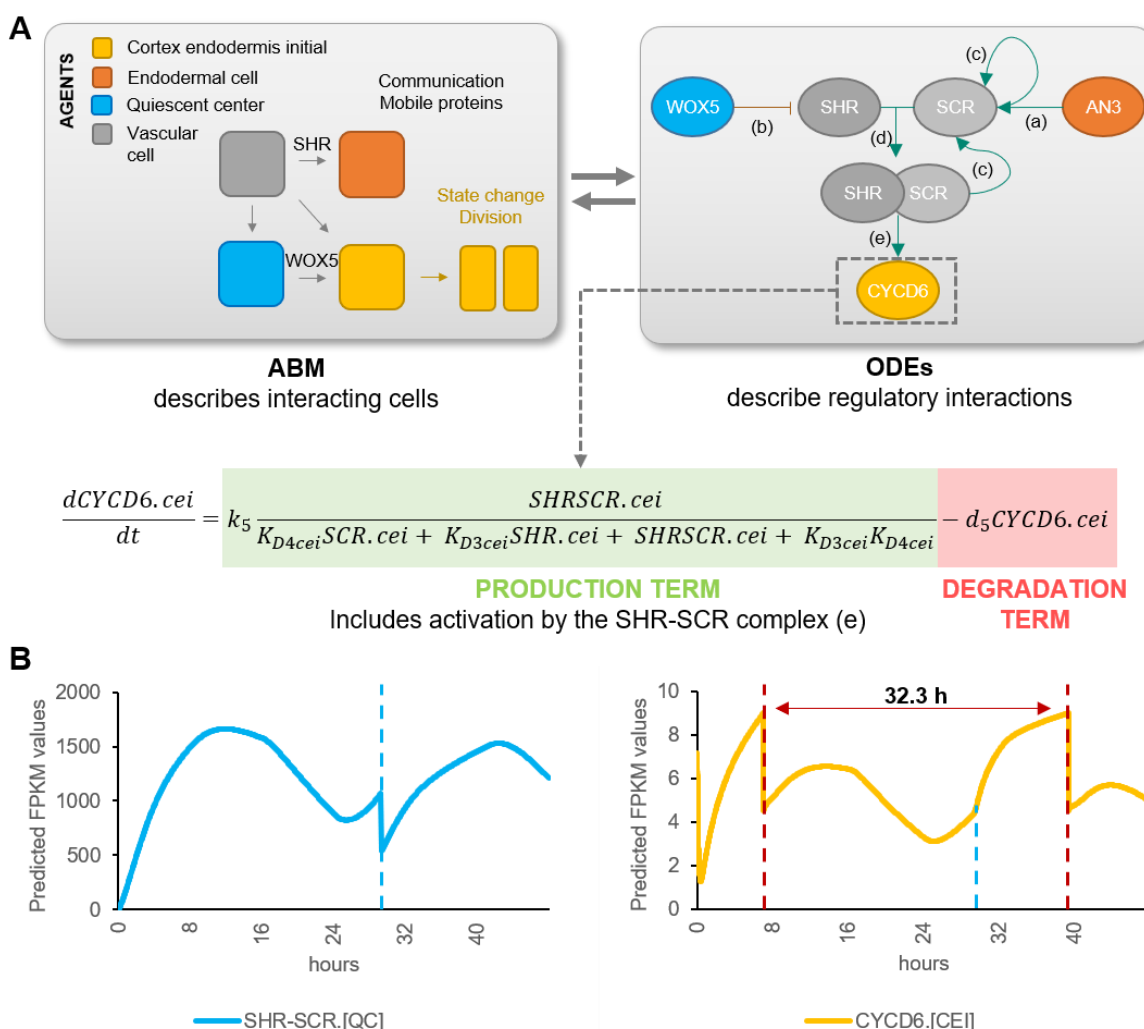
161 Figure 3 – Phenotypic analysis of *an3*. (A) Percentage of divided and undivided CEI cells in wild-type (Col) and *an3* roots. (B)  
162 The number of endodermal and cortex cells expressing pCYCD6;1:GUS-GFP in *an3*xpCYCD6;1:GUS-GFP roots. (C) Confocal  
163 image of *an3*xpCYCD6;1:GUS-GFP root. Data are presented as mean  $\pm$  SEM. \* =  $p < 0.05$  (A, B: Wilcoxon Chi-square test).

#### 164 A hybrid model to dynamically simulate and predict stem cell divisions

165 If AN3 and WOX5 are indeed key regulators for CEI divisions, we would expect that their temporal  
166 expression influences CEI divisions in a cell-type specific manner. To gain insight into the system-level  
167 regulation of CEI stem cell divisions, we modeled the expression of *CYCD6;1* and its direct and indirect  
168 upstream regulators: SHR, SCR, WOX5, and AN3 (Fig 1C, Fig 3B) (Sozzani et al., 2010). For this we  
169 developed a hybrid model that combines agent-based modeling aspects with ODEs. Specifically, we  
170 included four different cell types or “agents” (QC, CEI, vascular initial, and endodermal cell) and  
171 constructed ODEs of the genes for each cell type that are able to recapitulate the dynamics of the  
172 upstream regulatory interactions at a molecular scale. The cells/agents interact through the movement  
173 of SHR and WOX5 and change state (i.e. divide) upon changes in the expression of specific proteins.  
174 For example, when *CYCD6;1* exceeds a certain abundance, the CEI will divide. Each time a cell divides  
175 (an agent changes state), corresponding protein abundances are halved. As such, we were able to  
176 exchange information bidirectionally, from molecular to cellular scale and from cellular to molecular  
177 scale. To implement this hybrid model we used SimBiology to model, simulate, and analyze dynamic  
178 systems that allows for rapid model optimization and provides an intuitive visualization of the model  
179 (The MathWorks, 2019).

180 To analyze the temporal expression dynamics of *CYCD6;1* linked to CEI divisions, and to understand  
181 the regulatory role of WOX5 and AN3 in controlling the *CYCD6;1* dynamics, we used ODEs to generate  
182 a quantitative model that describes the dynamics of four key transcriptional regulators of *CYCD6;1*,

183 namely WOX5, AN3, SHR, and SCR. In our ODE systems, each ODE included a degradation term and a  
184 production term that depended on its upstream regulations. The included regulations are depicted in  
185 Figure 4 and are: (a) the inhibition of *SHR* by WOX5 in the vasculature (Clark, Fisher, et al., 2020), (b)  
186 the activation of *SCR* by the SHR/SCR complex in the endodermis, CEI, and QC (Heidstra et al., 2004;  
187 Helariutta et al., 2000), (c) the activation of *SCR* by AN3 (Ercoli et al., 2018), and (d) the activation of  
188 *CYCD6;1* by the SHR/SCR complex in the CEI (Fig 4A) (Sozzani et al., 2010). As the upstream  
189 transcriptional regulations of WOX5 and AN3 are unknown, we modeled their expression based on  
190 previously published data of *WOX5* and *AN3* expression over time in the SCN (Clark et al., 2019).  
191 Additionally, we included ODEs that model the movement of WOX5 from the QC to the vasculature  
192 initials (Supplemental Table 3), different diffusion rates of SHR from the vascular initials to the  
193 endodermis and QC (Clark, Fisher, et al., 2020), the SHR/SCR complex formation, and the oligomeric  
194 states of WOX5 and AN3. The oligomeric states of AN3 and WOX5 were experimentally determined  
195 using scanning FCS (Supplemental Fig 3). Specifically, we performed Number and Brightness (N&B) on  
196 *an3* or *wox5* roots expressing pAN3:AN3-GFP or pWOX5:WOX5-GFP translational fusion, respectively.  
197 We found that both AN3 and WOX5 primarily exist as a monomer (98.67% and 96.01%, respectively)  
198 with a very small amount of dimerization (1.33% and 3.99%, respectively) (Supplemental Fig 3). Thus,  
199 we fixed the oligomeric state of AN3 and WOX5 as monomers in our ODE model. As SHR and SCR  
200 dimers show a similar expression pattern as the monomers (Clark, Fisher, et al., 2020), we simplified  
201 the model and reduced the number of parameters by modeling the SHR and SCR monomer and dimer  
202 as one variable. Despite this simplification and the experimental estimation of several parameters, the  
203 number of parameters in the hybrid model still reaches over 30 as a result of its multiscale nature  
204 spanning both cellular and molecular interactions. To further reduce the number of parameters that  
205 needed to be estimated, the most influential parameters were identified with a sensitivity analysis  
206 (Sobol', 2001) (Supplemental Table 4, Supplemental Fig 4).



223 analyzing confocal images of the QC, CEI, and endodermal cells of pSCR:SCR-GFP for corrected total  
224 cell fluorescence (CTCF) at 5 days 16 hours (Supplemental Fig 5A,B). Model simulations showed that  
225 the cell-specific networks ensured robust stability of cellular behavior, such as cell division regulation  
226 (Fig 4B). The agent-based rules for cell division were set based on SHR/SCR complex and WOX5  
227 expression for the QC and CYCD6;1 expression for the CEI (Supplemental Fig 6). Our hybrid model was  
228 able to capture a dynamic expression pattern for the SHR/SCR complex, with high expression at 4 days  
229 8 hours and 5 days 16 hours. In contrast, WOX5 shows a low expression at these time points  
230 (Supplemental Fig 5C). The first peak of SHR/SCR expression at 4 days 8 hours was previously shown in  
231 an ODE model, while the second peak occurred, compared to our model, earlier at 5 days 8 hours  
232 (Clark, Fisher, et al., 2020). Model predictions show that the fine balance between low expression of  
233 the SHR/SCR complex and WOX5 simulates a QC cell division at 5 days 5 hours. Indeed, 5- and 6-day-  
234 old plants show an increase in QC divisions compared to 4-day-old plants (Supplemental Fig 5D).  
235 Additionally, CEI divisions are predicted to occur at 4 days 8 hours and 5 days 16 hours (Fig 4B). We  
236 observed an increased percentage of divided CEIs in 5-day-old roots compared to 4-day-old roots,  
237 however, an increase was not visible in 6-day-old roots compared to 5-day-old roots (Fig 1D, Fig 3A).  
238 We found that the rate of CEI divisions within our model was influenced by the QC division. For  
239 example, the change in WOX5 expression upon QC division impacts SHR expression and thus indirectly  
240 the SHR/SCR complex formation. The SHR/SCR complex, in turn, directly regulates CYCD6;1 expression  
241 which triggers CEI divisions. As such, CEI divisions are temporally correlated with the QC divisions. To  
242 test the involvement of protein movement in the interdependence of QC and CEI divisions, we  
243 quantified the CEI divisions in a *wox5xpWOX5:WOX5-3xGFP* line where WOX5 movement is inhibited  
244 (Berckmans et al., 2020). The number of divided CEIs were decreased in the *wox5xpWOX5:WOX5-*  
245 *3xGFP* line, potentially the result from WOX5 repressing activities on SHR in the vascular initials  
246 (Supplemental Fig 5E,F) and, consequently, reduced levels of SHR decreases CYCD6;1 activation in the  
247 CEIs (Koizumi et al., 2012). The distinct phenotype of *wox5xpWOX5:WOX5-3xGFP* line compared to the  
248 *wox5* mutant phenotype, which shows an increased number of divided CEIs, and the complemented  
249 *wox5xpWOX5:WOX5-xGFP*, suggests that WOX5 movement is key for proper CEI divisions. Taken  
250 together, our results suggest a QC division at 5 days 5 hours resulting from high SHR/SCR and low  
251 WOX5 concentrations, CEI divisions at 4 days 8 hours and 5 days 16 hours resulting from high CYCD6;1  
252 concentrations, and an interdependence between CEI divisions and QC divisions.

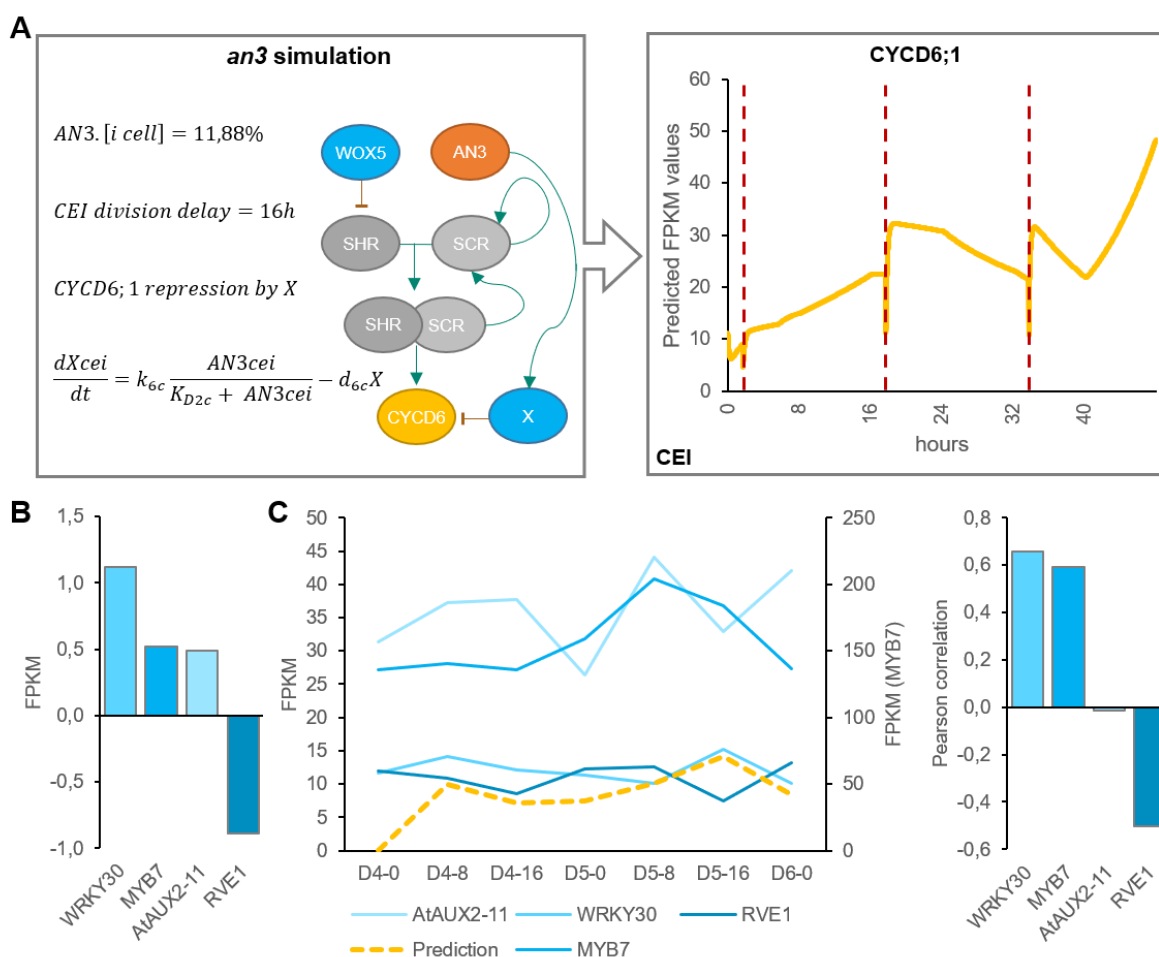
253 **The hybrid model partially captures systems behavior in response to molecular perturbations**

254 The regulatory network underlying the hybrid model can recapitulate the QC and CEI divisions in WT  
255 conditions. However, to further validate the model, we simulated the loss-of-function of *wox5* and *an3*  
256 and evaluated the expression patterns as well as CEI division dynamics. Based on transcriptome data

257 of *wox5* and *an3*, we calculated an 99.53% and 88.12% reduction of *WOX5* and *AN3* expression in their  
258 respective loss-of-function lines (Supplemental Fig 7). As such, the initial expression levels of *WOX5*  
259 and *AN3* were set to 0.47% and 11.88% in the mutant simulation as compared to the values in a WT  
260 situation, respectively.

261 Model simulations of *wox5* loss-of-function predicts an additional CEI division between 4 and 5 days  
262 compared to WT, which coincides with an increase in divided CEI cells at 4 days in *wox5* (Supplemental  
263 Fig 8A, Fig 1D). The additional division is most likely the result of the removal of *WOX5* repression on  
264 *SHR* in the vascular initials leading to an accelerated accumulation of *SHR/SCR* complex in the CEI. An  
265 overall increase in *SHR/SCR* in the CEI was not predicted by the model (Supplemental Fig 9B), and  
266 accordingly, CEI-specific transcriptomics and protein quantifications in the CEI of the *wox5* mutant did  
267 not show an increased *SHR* expression (Supplemental Table 2, Supplemental Fig 9A). The simulations  
268 of the *an3* loss-of-function predict the depletion of *SCR* in the QC, CEI, and endodermal cell compared  
269 to WT (Supplemental Fig 8B). This decrease in *SCR* expression has been shown within the QC (Ercoli et  
270 al., 2018). However, the CEI and endodermis still showed high levels of *SCR* when a repressor version  
271 of *AN3* is expressed in the *SCR* reporter line (Ercoli et al., 2018), which is in contrast to the model  
272 predictions. As such, the regulation of *CYCD6;1* by *AN3* in the CEI may not be established via *SCR* but  
273 another unknown mechanism. We hypothesized that *AN3* is regulating an additional factor that  
274 represses *CYCD6;1*. For this, we added an unknown factor X that is activated by *AN3* and represses  
275 *CYCD6;1*, removed the *AN3* activation of *SCR*, updated the ODEs within the CEI agent accordingly, and  
276 re-estimated 4 former and 2 new parameters (see Materials and Methods) (Supplemental Table 7,8).  
277 During model optimization, an additional rule that ensured a fixed minimum time between two CEI  
278 divisions was implemented to overcome overproliferation in the model (see Materials and Methods).  
279 By adding competition between a repressor, transcriptionally activated by *AN3*, and the *SHR/SCR*  
280 direct regulation of *CYCD6;1*, the model was able to accurately capture the CEI divisions in a wild-type  
281 situation as well as in an *an3* mutant background (Fig 5A). Notably, by adding the repressor to the  
282 model, the CEI division time interval shortened to 23.3 hours (Supplemental Fig 10). To identify  
283 potential candidates as a repressor downstream of *AN3*, we performed genome-wide expression  
284 analysis on *an3* meristematic root tissue (Supplemental Table 9). In total 1013 genes were differentially  
285 expressed ( $q < 0.05$ ) including 67 TFs of which 4 TFs were shown to interact with TOPLESS (TPL), a  
286 known transcriptional corepressor (Causier et al., 2012) (Fig 5B). Of these 4 transcriptional repressors,  
287 WRKY30 and MYB7 showed the highest expression correlation with the model prediction (Fig 5C).  
288 WRKY30 and MYB7 were also identified as a downstream target of *AN3* in a tandem chromatin affinity  
289 purification (TChAP) experiment (Vercruyssen et al., 2014). AtAUX2-11 and RVE1 showed no  
290 correlation and anti-correlation with the model predictions, respectively. As such, we propose WRKY30

291 or MYB7 as the putative downstream target of AN3 and repressor of *CYCD6;1* in the model. Our hybrid  
 292 model suggests that the regulation of CEI divisions by AN3 does not occur through its regulation of  
 293 *SCR*. Model predictions propose an unknown repressor activated by AN3 that is able to control *CYCD6;1*  
 294 expression. Overall, we modeled systemic behavior and predicted *SCR*, *SHR*, *WOX5*, *AN3*, and *CYCD6;1*  
 295 cell-type-specific protein concentrations as well as QC and CEI division dynamics.



296  
 297 Figure 5 – Mathematical modeling of CEI behavior in the *an3* mutant background. (A) Left panel indicates the modifications  
 298 made to the model. Right panel shows the *CYCD6;1* expression during the *an3* simulation in the CEI agent. Red dotted lines  
 299 indicate a division. (B) The expression values of transcriptional repressors within the *an3* transcriptome dataset identified  
 300 through overlap with the TOPLESS interactome. (C) The expression of the four identified transcriptional repressors in the *an3*  
 301 mutant within the stem cell time course (left) and Pearson correlation with the model predicted FPKM values (right). FC =  
 302 fold change, CEI = cortex endodermal initial.

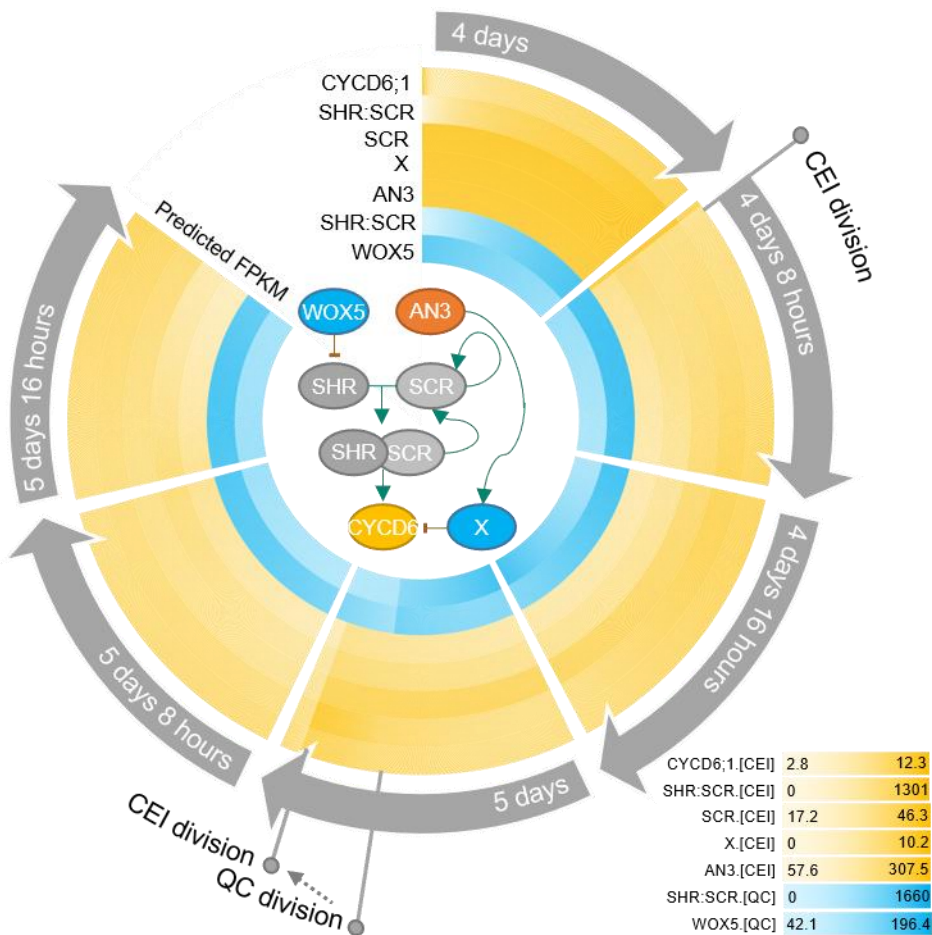
### 303 Discussion

304 Plants are multiscale systems in which cellular processes, such as the divisions of cells, occur at a  
 305 different timing than molecular processes, such as protein movement. To understand these multiscale  
 306 systems and connect molecular dynamics with phenotypic changes, models that take into account  
 307 multiple scales are becoming increasingly important. We have proposed an ODE and agent-based

308 hybrid model that allows for the exchange of information across biological scales, from a molecular  
309 scale (i.e. regulatory interactions at single cell level) to a cellular scale (i.e. division of stem cells). As  
310 such, protein abundances have a direct influence on cell divisions and vice versa. Additionally, the cell  
311 divisions within the model could be triggered by the expression dynamics of regulatory networks  
312 within each cell.

313 In the *Arabidopsis* root stem cell niche (SCN), the different stem cell types and the quiescent center  
314 (QC) are positioned in a highly regular and well-characterized organization. The asymmetric divisions  
315 of these organized stem cells form all cell- and tissue-types of *Arabidopsis* root and are controlled by  
316 dynamic, yet robust, regulatory signaling mechanisms. Several transcription factors (TFs) have been  
317 identified in a cell-type specific context to regulate stem cell divisions. For example, SHR and SCR are  
318 known to activate *CYCD6;1* in the cortex endodermis initials (CEI) (Sozzani et al., 2010) and, in this  
319 study, we propose a non-cell autonomous function for WOX5 in the regulation of CEI divisions. The  
320 extended expression pattern of *CYCD6;1* into both the endodermis and cortex cells proximal of the CEI  
321 in *wox5* has, to our knowledge, not yet been observed. However, treating wild-type plants with auxin  
322 results in an extended *CYCD6;1* expression pattern solely into the endodermis, coinciding with  
323 additional periclinal divisions (Cruz-Ramírez et al., 2012). Similarly, increased *CYCD6;1* expression into  
324 the endodermis in the upper ground tissue was observed in an RNAi line of MEDIATOR 31 (MED31)  
325 (Zhang et al., 2018). However, the function of key proteins, such as WOX5 and SHR, on a system-level  
326 scale is unknown and key questions remain: How do key regulatory proteins coordinately regulate  
327 stem cell divisions? What set of rules and parameters govern these complex systems? In this study, we  
328 have used a multiscale hybrid model to advance research that aims to connect molecular dynamics  
329 with phenotypic changes. The connection between regulatory inputs and cellular behavior, such as cell  
330 division, is highly complex and requires computational models to generate and test hypotheses about  
331 the rules governing these cellular behaviors. The hybrid model allowed us to describe complex  
332 systemic behavior by combining: (1) discrete agent-based modeling aspects to incorporate cell-  
333 specificity and allow for cell divisions through simple rules, and (2) continuous ODE models to describe  
334 the expression dynamics of the included proteins. Including interactions between agents/cells is critical  
335 to fully address system-level problems and replicate observable behaviors. Questions about how  
336 mobile proteins affect phenotypic changes can be addressed by instructing agents/cells to  
337 communicate effectively in a model. To note, this model is not attempting to simulate and predict the  
338 division plane or direction. The ODE and agent-based hybrid model includes short range signals  
339 allowing for cell-to-cell communication. The mobile proteins, WOX5 and SHR, non-cell-autonomously  
340 regulate the expression of downstream proteins in specific cell types and allow for the communication  
341 between these cell types. WOX5 proteins can move to the neighboring vascular initials and CEI cells

342 and SHR proteins move to the QC, CEI, and endodermal cells. Scanning FCS was used to quantify the  
343 diffusion coefficient of WOX5 and SHR to include into the model (Supplemental Table 7) (Clark et al.,  
344 2016; Clark, Van den Broeck, et al., 2020). As such, the model predicted an additional CEI division in  
345 *wox5* mutant as a result of the non-cell-autonomous regulation of *SHR* by WOX5 in the vascular initials  
346 and the movement of SHR to the CEI. Importantly, the inclusion of cell-to-cell communication into the  
347 model was crucial to accurately model stem cell division dynamics and contributed towards a better  
348 understanding of the rules underlying cellular behavior.



349

350 Figure 6 – Overview of stem cell division dynamics. Circular heatmap of the predicted FPKM of *WOX5*, *SHR/SCR*, *AN3*,  
351 *CYCD6;1*-repressor *X*, *SCR*, and *CYCD6;1* over time from 4-day-old roots up to 6-day-old roots. The yellow and shades are  
352 predicted FPKM in the CEI and the QC, respectively. CEI and QC divisions are marked upon the heatmap. In the middle of the  
353 circular heatmap, a network with the known and predicted regulatory interactions between these key proteins is drawn.  
354 Green and red arrows represent activation and repression, respectively.

355 Overall, our computational models and approach was aimed at making predictions about the rules of  
356 stem cell divisions that lead to testable hypotheses and assist in making future decisions. Accordingly,  
357 since the model suggested that the CEI-specific role of AN3 was not established through the regulatory  
358 interaction with SCR, we implemented a transcriptional repressor regulated by AN3, a non-intuitive  
359 aspect, to simulate the additional CEI divisions as found in an *an3* background. Four candidate

360 transcriptional repressors (Causier et al., 2012) downstream of AN3 and upstream of *CYCD6;1* were  
361 proposed based on transcriptome analysis, of which *WRKY30* and *MYB7* showed the highest  
362 correlation with model predictions and were identified as a downstream target of AN3 in a TChAP  
363 experiment (Vercruyssen et al., 2014). Even though, since this is outside the scope of the study, the  
364 roles of these four TFs in regulating stem cell division within the SCN remains elusive, our integrative  
365 multiscale model allowed us to both 1) predict cellular behavior in normal conditions; and 2) capture  
366 CEI division dynamics in response to perturbations. Thus, by combining continuous models to describe  
367 cell-specific regulatory networks and agent-based rules, systemic behavior was modeled and led to a  
368 deeper understanding of the regulatory rules governing cell division.

369 **Materials and methods**

370 *Plant material and growth conditions*

371 The *wox5* and *an3* loss-of-function lines, pAN3:AN3-GFP, 35S-AN3-GFP, pWOX5:WOX5-GFP  
372 pCYCD6;1:GUS-GFP, and *wox5* x pCYCD6;1:GUS-GFP are previously described in (Clark, Fisher, et al.,  
373 2020; Ercoli et al., 2018; Sozzani et al., 2010; Vercruyssen et al., 2014). *an3* x pCYCD6;1:GUS-GFP was  
374 generated by crossing *an3* with pCYCD6;1:GUS-GFP. Homozygous plants were selected by PCR using  
375 the SALK LB primer and the AN3-specific oligos 5'-ATTACGACACAACCTTGGAGCC-3' and 5'-  
376 TTTGTGGTCCGAAACAAACATC-3'. All lines were upscaled with their corresponding wild type.

377 For imaging and root growth assays, seeds were dry sterilized using fumes produced by a solution of  
378 100% bleach and 1M hydrochloric acid. The seeds were plated on square Petri dishes with solid (10 g/L  
379 agar, Difco<sup>TM</sup>) 1X MS (Murashige and Skoog) medium supplemented with 1% sucrose and stratified for  
380 2 days at 4°C. The plates were grown vertically at 22°C in long-day conditions (16-hrs light/ 8-hrs dark)  
381 for 4, 5, 6, or 7 days as indicated in the figures. At least three biological replicates of 10 to 20 plants  
382 were performed for the root growth assays and confocal images. The different lines were always grown  
383 together on one plate with the appropriate control line. For RNAseq experiments, seeds were wet  
384 sterilized using 50% bleach, 100% ethanol, and water. Seeds were imbibed and stratified for 2 days at  
385 4°C. Next, the seeds were plated with high density on Nitex mesh squares on top of solid 1X MS  
386 medium with 1% sucrose. Seeds were plated and grown vertically at 22°C in long-day conditions.

387 *Root growth assays*

388 At 3, 4, 5, 6, and 7 days, the primary root length was marked. At 7 days, a picture of the marked square  
389 plates was taken and the root length was measured using the software program ImageJ version 1.45  
390 (National Institutes of Health; <http://rsb.info.nih.gov/ij/>). For the statistical analysis of the root growth  
391 assays, Student's t-tests were performed on the average of each biological replicate.

392 *Confocal imaging, pCF analysis, and Number & Brightness (N&B)*

393 Confocal microscopy was conducted using a Zeiss LSM 710 or 880 on 4, 5, or 6 day-old root tips. The  
394 488nm and 570nm lasers were used for green and red channel acquisition, respectively. Propidium  
395 iodide (10 $\mu$ M, Calbiochem) was used to stain cell walls and mPS-PI staining was used to visualize starch  
396 granules. For the N&B acquisition, 12-bit raster scans of a 256x256 pixel region of interest were  
397 acquired with a pixel size of 100nm and a pixel dwell time of 12.61 $\mu$ s as described in (Clark et al., 2016;  
398 Clark & Sozzani, 2017). For pair correlation function (pCF) acquisition, 100000 12-bit line scans of a  
399 32x1 pixel region of interest were acquired with a varying pixel size and a pixel dwell time of 8.19 $\mu$ s as  
400 described in (Clark et al., 2016; Clark & Sozzani, 2017). Heptane glue was used during N&B and pCF  
401 acquisition to prevent movement of the sample as described in (Clark et al., 2016; Clark & Sozzani,  
402 2017).

403 Analysis of confocal images for corrected total cell fluorescence (CTCF) measurements was performed  
404 as described previously (Clark et al., 2019). Analysis of the raster scans acquired for N&B and the line  
405 scans for pCF was performed using the SimFCS software (<https://www.lfd.uci.edu/globals/>). For N&B,  
406 the 35S:GFP line was used to normalize the background region of the image (S-factor of 2.65) and  
407 determine monomer brightness (brightness of 0.26). A 128x128 region of interest was used on all  
408 images to measure oligomeric state specifically in the QC. For pCF, each line scan image was analyzed  
409 with three different pixel distances (8, 10 and 12, or 7, 9 and 11) in both a left-to-right (movement  
410 from QC to CEI) and a right-to-left scanning direction (movement from CEI to QC). For each technical  
411 replicate of a line scan image, a qualitative Movement Index (MI) was assigned based on the detection  
412 of movement in the carpet (arch pattern, MI=1) or not (no arch pattern, MI=0) (Clark et al., 2016; Clark  
413 & Sozzani, 2017). The technical replicates were then averaged for each biological replicate. The  
414 pWOX5:WOX5:GFP images were analyzed separately in both directions.

415 *RNAseq analysis and network inference*

416 Three hundred to five hundred mg of pWOX5:erGFP, pCYCD6:GUS-GFP, and *wox5* x pCYCD6:GUS-GFP  
417 seeds were wet sterilized and plated for each of the four biological replicate. After 5 days of growth,  
418 approximately 1mm of the root tip was collected and protoplasted as described (Birnbaum et al.,  
419 2005). GFP positive and negative cells were collected using a MoFlo cell sorter into a vial containing a  
420 solution of beta-mercaptoethanol and RLT buffer. RNA was extracted using the Qiagen RNeasy Micro  
421 kit. Libraries were prepared using the SMART-Seq v3 Ultra Low RNA Input Kit for Sequencing and the  
422 Low Library Prep Kit v1 from Clontech. For the *an3* RNAseq experiment, ~5 mm of *an3* and WT root  
423 tips were collected for each of the three biological replicates. RNA was extracted using the Qiagen  
424 RNeasy Micro kit and libraries were prepared using the NEBNext Ultra II RNA Library Prep Kit for  
425 Illumina (New England BioLabs). All libraries were sequenced on an Illumina HiSeq 2500 with 100 bp  
426 single-end reads.

427 Gene expression analysis of raw RNA-seq data and subsequent GRN inference was performed using  
428 the TuxNet interface (Spurney et al, 2019). Specifically, TuxNet uses ea-utils fastq-mcf (Aronesty, 2011,  
429 Aronesty, 2013) for preprocessing, hisat2 (Kim et al, 2015) for genome alignment, and Cufflinks  
430 (Trapnell et al, 2012) for differential expression analysis. To infer a gene regulatory network (GRN) and  
431 predict the causal relationships of genes regulating CEI identity, differentially expressed genes (DEGs)  
432 were identified using  $q < 0.05$  as our selection criteria, when performing pairwise comparisons  
433 between GFP negative cells from pWOX5:erGFP and GFP positive cells from pCYCD6:GUS-GFP or *wox5*  
434 x pCYCD6:GUS-GFP. Within the TuxNet interface, RTP-STAR (Regression Tree Pipeline for Spatial,  
435 Temporal, and Replicate data) was used for all network inference. The pipeline consists of three parts:  
436 spatial clustering using the k-means method, network inference using GENIE3, and edge sign  
437 (activation or repression) identification using the first order Markov method. TuxNet is available at  
438 <https://github.com/rspurney/TuxNet> and video tutorials regarding installation, analysis, and network  
439 inference are freely available at <https://rspurney.github.io/TuxNet/>. The network was visualized in  
440 Cytoscape® 3.8.0 (Shannon et al., 2003).

441 *Node impact analysis*

442 Each node from the network receives a weight between 1 and 2:

443 
$$weight(N) = w = 1 + \frac{O}{O_{max}}$$

444 Nodes with a high outdegree ( $O$ ) are considered to be more impactful within the network and will thus  
445 receive a high weight. The impact of a node within the network topology is calculated based on the  
446 weighted first neighbors:

447 
$$R = ASPL \times \sum_{1 \text{ to } O}^i w_i + A \times \sum_{1 \text{ to } I}^i w_i$$

448 
$$A = \frac{\text{Nodes (outdegree} > 0\text{)}}{\text{Nodes}}$$

449 where  $R$  = Robustness,  $ASPL$  = Average Shortest Path Length,  $O$  = outdegree, and  $I$  = indegree. A scale-  
450 free network will have a low  $A$ , while a scale-rich network will have a high  $A$ , allowing for the indegree  
451 to contribute more to the impact of a node. Because the first neighbors are weighted in regards to  
452 their outdegree, genes with a lower outdegree can still have a large impact if its neighbors have a high  
453 outdegree and the gene is thus centrally located. Genes with a large number of cascading targets that  
454 are 2 or more nodes away will have a higher ASPL and thus a higher scaled outdegree weight,  
455 accurately reflecting the hierarchical importance of the source gene itself and its first neighbors  
456 targets.

457 *Shiny app: Node Analyzer*

458 To calculate necessary network statistics such as outdegree and indegree in Cytoscape® 3.8.0 (Shannon  
459 et al., 2003), select Tools -> Analyze Network, check the Analyze as Directed Graph if applicable, and  
460 then press OK to perform the analysis. To export node and edge files from Cytoscape, select File ->  
461 Export -> Table to File, and then choose default edge or default node in the 'Select a table to export'  
462 dropdown. Press OK to export each file. Import the node and edge table files into the corresponding  
463 prompts (Fig 2C) and press the Run Analysis button to calculate impact scores. Results can be  
464 downloaded as a table using the Download Results button. In addition to the impact scores, the  
465 application renders three plots for visualization: one plot with the impact score for each gene and two  
466 histograms with the indegree and outdegree.

467 The Node Analyzer user interface can be accessed online at  
468 <https://rspurney.shinyapps.io/nodeanalyzer/> or ran through R with scripts freely available at  
469 <https://github.com/rspurney/NodeAnalyzer>. Example datasets are also available via the GitHub link.

470 *Ordinary equations, parameter estimation, and sensitivity analysis*

471 Ordinary differential equations (ODEs) were developed to model the dynamics of CYCD6;1, its  
472 upstream regulators SHR and SCR, WOX5, and AN3 in three different cell types: endodermal cells, CEI,  
473 and QC. The regulatory interactions between these five proteins were modeled using Hill equation  
474 dynamics, and SHR-SCR complex formation is modeled using mass-action kinetics. SHR and WOX5  
475 diffusion are modeled using a linear term for gradient-independent diffusion. All proteins are assumed  
476 to have a linear degradation term. We modeled transcriptional regulation and protein expression in  
477 the same equation.

478 (1) **SHR**; for the upstream regulation of *SHR* in the vasculature, the repression by WOX5 was  
479 included (top equation) (Clark, Fisher, et al., 2020).

$$480 \frac{dSHR. [vasc]}{dt} = k_4 \frac{K_{D1vasc}}{K_{D1vasc} + WOX5. [vasc]} - d_4 SHR. [vasc]$$

481 (2) **SCR**; for the upstream regulation of *SCR* expression, we included the autoactivation by SCR  
482 itself (Cruz-Ramírez et al., 2012; Heidstra et al., 2004), the activation by the SCR-SHR complex  
483 (Heidstra et al., 2004), and the activation by AN3 (Ercoli et al., 2018). Each one of these  
484 regulations was assumed to be sufficient to induce *SCR* expression.

$$485 \frac{dSCR. [i\ cell]}{dt} = k_{3i} \left( \frac{K_{D4i} SCR. [i\ cell] + SSC. [i\ cell]}{K_{D3i} K_{D4i} + K_{D4i} SCR. [i\ cell] + K_{D3i} SHR. [i\ cell] + SSC. [i\ cell]} \right. \\ 486 \left. + \frac{AN3. [i\ cell]}{K_{D2i} + AN3. [i\ cell]} \right) - d_{3i} SCR. [i\ cell]$$

487 (3) **WOX5**; the production of WOX5 was assumed to be time-dependent as this produces the best  
488 model fit to the experimental data (top equation) (Clark, Fisher, et al., 2020).

489

$$\frac{dWOX5. [QC]}{dt} = k_{1qc} WOX5. [QC]$$

490 (4) **AN3**; the production of AN3 was assumed to be time-dependent as this produces the best  
491 model fit to the experimental data.

492

$$\frac{dAN3. [i\ cell]}{dt} = k_{2i} AN3. [i\ cell]$$

493 (5) **CYCD6;1**; for the upstream regulation of *CYCD6;1* expression, we included the activation by  
494 the SCR-SHR complex (Sozzani et al., 2010).

495

$$\frac{dCYCD6. [CEI]}{dt} = k_5 \frac{SSC. [CEI]}{K_{D4cei} SCR. [CEI] + K_{D3cei} SHR. [CEI] + SSC. [CEI] + K_{D3cei} K_{D4cei}} - d_5 CYCD6. [CEI]$$

496 It was shown that the different oligomeric forms and stoichiometries of SHR, SCR, and the SCR-SHR  
497 complex show a similar expression pattern (Clark, Fisher, et al., 2020). As such, the SHR and SCR  
498 oligomeric forms were modeled as one variable.

499 The interaction between the different agents/cell types is modeled using mass-action kinetics. The  
500 state change following division is modelled using simple agent-based rules. To simulate division of an  
501 agent, the capacity of the cell doubles, subsequently halving all proteins present.

502 (6) The cell types interact with each other through the movement of the regulatory proteins SHR  
503 and WOX5. The amount of SHR in the other cell types was determined by the movement of  
504 SHR (top equation). The amount of WOX5 in the vasculature was determined by the movement  
505 of WOX5 from the QC (bottom equation) (Fig 1).

506

$$\frac{dSHR. [i\ cell]}{dt} = a_i SHR. [vasc] - d_{12i} SHR. [i\ cell]$$

507

$$\frac{dWOX5. [vasc]}{dt} = a_{vasc} WOX5. [QC] - d_{1vasc} WOX5. [vasc]$$

508 (7) It was shown that the division of the QC cell correlates with the expression of WOX5 and the  
509 SCR-SHR complex (Clark, Fisher, et al., 2020).

510

$$if\ WOX5. [QC] \leq 100 \& SSC. [QC] \leq 1100 : \frac{Gene_{0\ to\ j}. [QC]}{2}$$

511 (8) We assumed that the division of the CEI cells is dependent on the expression of CYCD6;1  
512 (Sozzani et al., 2010).

513

$$if\ CYCD6. [CEI] \geq 9 : \frac{Gene_{0\ to\ j}. [CEI]}{2}$$

514 For the sensitivity analysis, the total Sobol effect index was calculated for each parameter value (Saltelli  
515 et al., 2010; Sobol', 2001). Parameter values were randomly sampled using Monte Carlo sampling to  
516 obtain 150 different values for each parameter. This analysis was repeated for 10 technical replicates.  
517 As such, for each parameter 170 (10 replicates x 17 ODEs) total Sobol effect indices were obtained. For  
518 each ODE and replicate the sensitivities were rescaled between 0 and 1 and then averaged across the  
519 17 ODEs. The obtained averaged sensitivities for each replicate were again averaged to retrieve the  
520 total Sobol effect index per parameter (Supplemental Table 4). The sensitive parameters were chosen  
521 as the parameters that had significantly higher Sobol indices than the lowest scoring parameter  
522 (K\_D2\_qc) using a student's t-test (p<0.01).

523 To estimate the sensitive parameters, the model was fitted onto extrapolated cell-type specific time  
524 course expression data (Supplemental Table 5). To generate this cell-types specific time course  
525 expression data, FPKM values in the QC, CEI and vascular initials at 5 days were obtained from Clark et  
526 al, and the endodermis specific FPKM values at 5 days were obtained from Li et al (Clark et al., 2019;  
527 Li et al., 2016). Using the fold changes of a time course dataset from the root stem cell niche every 8  
528 hours from 4 to 6 days (Clark et al., 2019) and the FPKM values at 5 days for the specific cell types, we  
529 were able to extrapolate cell-type specific time course expression values (Supplemental Table 5).  
530 Simulated annealing and Latin hypercube sampling as described in (Clark, Fisher, et al., 2020) produced  
531 40 sets parameter estimates (Supplemental Table 6). The average of these parameter estimates was  
532 used for the model simulations. The remaining sensitive parameters were set to a constant value from  
533 the corresponding estimated parameter in (Clark, Fisher, et al., 2020). The value of non-sensitive  
534 parameters was selected based on similar values of the model described in (Clark, Fisher, et al., 2020).  
535 The production terms for WOX5 (k1\_qc) and AN3 (k2\_qc, k2\_cei, k2\_endo) were set to a constant value  
536 at each time point to minimize the error between the model and the time course expression data. The  
537 diffusion coefficients of SHR (a\_qc, a\_cei) and WOX5 (b\_qc) were experimentally determined from RICS  
538 experiments (Supplemental Table 3) (Clark, Fisher, et al., 2020).

539 The following changes were made in the regulatory network underlying the CEI divisions to reflect the  
540 *an3* loss-of-function in the hybrid model:

541 (1) **Factor X**; for the upstream regulation of the unknown repressor X in the CEI agent, the  
542 activation by AN3 was included.

$$543 \frac{dX. [CEI]}{dt} = k_{6cei} \frac{AN3. [CEI]}{K_{D2cei} + AN3. [CEI]} - d_{6cei} X. [CEI]$$

544 (2) **CYCD6;1**; for the upstream regulation of *CYCD6;1* expression, we added the repression of  
545 factor X in addition to the activation by the SCR-SHR complex (Sozzani et al., 2010).

546 
$$\frac{dCYCD6.[CEI]}{dt} = k_5 \left( \frac{SSC.[CEI]}{K_{D4cei}SCR.[CEI] + K_{D3cei}SHR.[CEI] + SSC.[CEI] + K_{D3cei}K_{D4cei}} \right.$$

547 
$$\left. + \frac{K_{D6cei}}{K_{D6cei} + X.[CEI]} \right) - d_5CYCD6.[CEI]$$

548 (3) **SCR**; for the upstream regulation of *SCR* expression in the CEI and endodermal agent, we  
549 included the autoactivation by *SCR* itself (Cruz-Ramírez et al., 2012; Heidstra et al., 2004), the  
550 activation by the *SCR-SHR* complex (Heidstra et al., 2004), and removed the activation by *AN3*  
551 (Ercoli et al., 2018).

552 
$$\frac{dSCR.[i\ cell]}{dt} = k_{3i} \frac{K_{D4i}SCR.[i\ cell] + SSC.[i\ cell]}{K_{D3i}K_{D4i} + K_{D4i}SCR.[i\ cell] + K_{D3i}SHR.[i\ cell] + SSC.[i\ cell]} - d_{3i}SCR.[i\ cell]$$

553 (4) To avoid uncontrollable division within the CEI, the CEI agent was subjected to an additional  
554 rule that ensured a minimum time of 16h between successive divisions ( $\Delta t$ ).

555 
$$if\ CYCD6.[CEI] \geq 9\ \& \Delta t > 16 : \frac{Gene\ to\ j.[CEI]}{2}$$

556 Four existing parameters (*k3\_endo*, *d3\_endo*, *k3\_cei* and *k5\_cei*) and two new parameters (*k6\_cei*,  
557 *d6\_cei*) were re-estimated in the same manner as described above and produced 20 sets parameter  
558 estimates (Supplemental Table 8). For the remaining parameters the same value as the initial hybrid  
559 model was used.

560 All parameters for the initial and adjusted model are listed in supplemental table 7. To simulate the  
561 hybrid models, the initial values were set as the 4D FPKM values from the extrapolated time course  
562 data. For factor X, the *SHR/SCR* complex, and very lowly expressed genes (e.g. *WOX5* in the vascular  
563 initials) the initial value was zero. To simulate *wox5* loss-of-function the initial value of *WOX5* was set  
564 to 0.47% (Supplemental Fig 7). To simulate *an3* loss-of-function the initial value of *AN3* in all three  
565 agents, was set to 11.88% (Supplemental Fig 7). ODE45 was used as the ODE solver within SimBiology.

#### 566 *Data and Coding Availability*

567 All sequencing data are available on GEO at:

- 568 - <https://www.ncbi.nlm.nih.gov/geo/query/acc.cgi?acc=GSE155462>: access token atqloyuybzufhon  
569 - <https://www.ncbi.nlm.nih.gov/geo/query/acc.cgi?acc=GSE155463>: access token ohmtgiedvcdrfu

570 MATLAB code used for the hybrid model is available at  
571 [https://github.com/LisaVdB/Hybrid\\_model\\_CEI\\_division](https://github.com/LisaVdB/Hybrid_model_CEI_division). R-code used to develop the Shiny  
572 application is available at <https://github.com/rsurney/NodeAnalyzer>.

#### 573 **Acknowledgements**

574 We thank Dr. Kensuke Kawade for *an3* seeds, Dr. Javier F. Palatnik for the pAN3:AN3-GFP seeds, Dr.  
575 Dirk Inzé for the p35S:AN3-GFP seeds, and Dr. Thomas Laux for pWOX:WOX5-GFP seeds.

576 **Author Contributions**

577 L.V.d.B., A.P.F., and R.S. conceived and designed the study. L.V.d.B. and R.J.S. conducted the  
578 computational modeling. N.M.C. advised on the modeling. R.J.S designed the Shiny App. A.P.F.,  
579 L.V.d.B., T.T.N, I.M, and M.G gathered experimental data. L.V.d.B and A.P.F analyzed experimental  
580 data. L.V.d.B performed statistical analysis. L.V.d.B, A.P.F., R.J.S, and R.S wrote the manuscript and all  
581 authors contributed to correcting the manuscript.

582 **Financial Support**

583 This work was supported by the National Science Foundation (NSF) (CAREER MCB-1453130) (MCB-  
584 1856248) to RS; Foundation for Food and Agriculture Research (FFAR) to RS; and NSF/Biotechnology  
585 and Biological Sciences Research Council (BBSRC) (MCB-1517058) to TAL and RS.

586 **Conflicts of Interest declarations in manuscripts**

587 The authors declare no conflict of interest.

588 **References**

- 589 Berckmans, B., Kirschner, G., Gerlitz, N., Stadler, R., & Simon, R. (2020). CLE40 Signaling Regulates  
590 Root Stem Cell Fate. *Plant Physiology*, 182(4), 1776 LP – 1792.  
591 <https://doi.org/10.1104/pp.19.00914>
- 592 Birnbaum, K., Jung, J. W., Wang, J. Y., Lambert, G. M., Hirst, J. A., Galbraith, D. W., & Benfey, P. N.  
593 (2005). Cell type-specific expression profiling in plants via cell sorting of protoplasts from  
594 fluorescent reporter lines. *Nature Methods*, 2(8), 615–619.  
595 <https://doi.org/10.1038/nmeth0805-615>
- 596 Canher, B., Heyman, J., Savina, M., Devendran, A., Eekhout, T., Vercauteren, I., Prinsen, E.,  
597 Matosevich, R., Xu, J., Mironova, V., & De Veylder, L. (2020). Rocks in the auxin stream: Wound-  
598 induced auxin accumulation and &lt;em&gt;ERF115&lt;/em&gt; expression synergistically drive  
599 stem cell regeneration. *Proceedings of the National Academy of Sciences*, 117(28), 16667 LP –  
600 16677. <https://doi.org/10.1073/pnas.2006620117>
- 601 Causier, B., Ashworth, M., Guo, W., & Davies, B. (2012). The TOPLESS interactome: a framework for  
602 gene repression in Arabidopsis. *Plant Physiology*, 158(1), 423–438.  
603 <https://doi.org/10.1104/pp.111.186999>
- 604 Cilfone, N. A., Kirschner, D. E., & Linderman, J. J. (2015). Strategies for Efficient Numerical  
605 Implementation of Hybrid Multi-scale Agent-Based Models to Describe Biological Systems.  
606 *Cellular and Molecular Bioengineering*, 8(1), 119–136. <https://doi.org/10.1007/s12195-014-0363-6>
- 608 Clark, N. M., Buckner, E., Fisher, A. P., Nelson, E. C., Nguyen, T. T., Simmons, A. R., de Luis Balaguer,  
609 M. A., Butler-Smith, T., Sheldon, P. J., Bergmann, D. C., Williams, C. M., & Sozzani, R. (2019).  
610 Stem-cell-ubiquitous genes spatiotemporally coordinate division through regulation of stem-  
611 cell-specific gene networks. *Nat Commun*, 10(5574).  
612 <https://doi.org/https://doi.org/10.1038/s41467-019-13132-2>
- 613 Clark, N. M., Fisher, A. P., Berckmans, B., Van den Broeck, L., Nelson, E. C., Nguyen, T. T., Bustillo-  
614 Avendaño, E., Zebell, S. G., Moreno-Risueno, M. A., Simon, R., Gallagher, K. L., & Sozzani, R.  
615 (2020). Protein complex stoichiometry and expression dynamics of transcription factors  
616 modulate stem cell division. *Proceedings of the National Academy of Sciences of the United  
617 States of America*. <https://doi.org/10.1073/pnas.2002166117>
- 618 Clark, N. M., Hinde, E., Winter, C. M., Fisher, A. P., Crosti, G., Blilou, I., Gratton, E., Benfey, P. N., &  
619 Sozzani, R. (2016). Tracking transcription factor mobility and interaction in Arabidopsis roots  
620 with fluorescence correlation spectroscopy. *ELife*, 5, 1–25. <https://doi.org/10.7554/elife.14770>
- 621 Clark, N. M., & Sozzani, R. (2017). *Measuring Protein Movement, Oligomerization State, and Protein–  
622 Protein Interaction in Arabidopsis Roots Using Scanning Fluorescence Correlation Spectroscopy  
623 (Scanning FCS) BT - Plant Genomics: Methods and Protocols* (W. Busch (ed.); pp. 251–266).  
624 Springer New York. [https://doi.org/10.1007/978-1-4939-7003-2\\_16](https://doi.org/10.1007/978-1-4939-7003-2_16)
- 625 Clark, N. M., Van den Broeck, L., Guichard, M., Stager, A., Tanner, H. G., Blilou, I., Grossmann, G., Iyer-  
626 Pascuzzi, A. S., Maizel, A., Sparks, E. E., & Sozzani, R. (2020). Novel Imaging Modalities Shedding  
627 Light on Plant Biology: Start Small and Grow Big. *Annual Review of Plant Biology*, 71, 789–816.  
628 <https://doi.org/10.1146/annurev-arplant-050718-100038>
- 629 Cruz-Ramírez, A., Díaz-Triviño, S., Blilou, I., Grieneisen, V. A., Sozzani, R., Zamioudis, C., Miskolczi, P.,  
630 Nieuwland, J., Benjamins, R., Dhonukshe, P., Caballero-Pérez, J., Horvath, B., Long, Y., Mähönen,  
631 A. P., Zhang, H., Xu, J., Murray, J. A. H., Benfey, P. N., Bako, L., ... Scheres, B. (2012). A bistable  
632 circuit involving SCARECROW-RETINOBLASTOMA integrates cues to inform asymmetric stem  
633 cell division. *Cell*, 150(5), 1002–1015. <https://doi.org/10.1016/j.cell.2012.07.017>

- 634 Dinneny, J. R., & Benfey, P. N. (2008). Plant stem cell niches: standing the test of time. *Cell*, 132(4),  
635 553–557. <https://doi.org/10.1016/j.cell.2008.02.001>
- 636 Ercoli, M. F., Ferela, A., Debernardi, J. M., Perrone, A. P., Rodriguez, R. E., & Palatnik, J. F. (2018). G1F  
637 Transcriptional Coregulators Control Root Meristem Homeostasis. *The Plant Cell*, 30(2), 347–  
638 359. <https://doi.org/10.1105/tpc.17.00856>
- 639 Fisher, A. P., & Sozzani, R. (2016). Uncovering the networks involved in stem cell maintenance and  
640 asymmetric cell division in the *Arabidopsis* root. *Current Opinion in Plant Biology*, 29, 38–43.  
641 <https://doi.org/https://doi.org/10.1016/j.pbi.2015.11.002>
- 642 Forzani, C., Aichinger, E., Sornay, E., Willemsen, V., Laux, T., Dewitte, W., & Murray, J. A. H. (2014).  
643 WOX5 suppresses CYCLIN D activity to establish quiescence at the center of the root stem cell  
644 niche. *Current Biology : CB*, 24(16), 1939–1944. <https://doi.org/10.1016/j.cub.2014.07.019>
- 645 Gallagher, K. L., & Benfey, P. N. (2009). Both the conserved GRAS domain and nuclear localization are  
646 required for SHORT-ROOT movement. *The Plant Journal : For Cell and Molecular Biology*, 57(5),  
647 785–797. <https://doi.org/10.1111/j.1365-313X.2008.03735.x>
- 648 Heidstra, R., Welch, D., & Scheres, B. (2004). Mosaic analyses using marked activation and deletion  
649 clones dissect *Arabidopsis* SCARECROW action in asymmetric cell division. *Genes &*  
650 *Development*, 18(16), 1964–1969. <https://doi.org/10.1101/gad.305504>
- 651 Helariutta, Y., Fukaki, H., Wysocka-Diller, J., Nakajima, K., Jung, J., Sena, G., Hauser, M.-T., & Benfey,  
652 P. N. (2000). The SHORT-ROOT Gene Controls Radial Patterning of the *Arabidopsis* Root through  
653 Radial Signaling. *Cell*, 101(5), 555–567. [https://doi.org/https://doi.org/10.1016/S0092-8674\(00\)80865-X](https://doi.org/https://doi.org/10.1016/S0092-8674(00)80865-X)
- 655 Huynh-Thu, V. A., Irrthum, A., Wehenkel, L., & Geurts, P. (2010). Inferring regulatory networks from  
656 expression data using tree-based methods. *PloS One*, 5(9), e12776.  
657 <https://doi.org/10.1371/journal.pone.0012776>
- 658 Koizumi, K., Hayashi, T., Wu, S., & Gallagher, K. L. (2012). The SHORT-ROOT protein acts as a mobile,  
659 dose-dependent signal in patterning the ground tissue. *Proceedings of the National Academy of  
660 Sciences*, 109(32), 13010 LP – 13015. <https://doi.org/10.1073/pnas.1205579109>
- 661 Krouk, G., Mirowski, P., LeCun, Y., Shasha, D. E., & Coruzzi, G. M. (2010). Predictive network modeling  
662 of the high-resolution dynamic plant transcriptome in response to nitrate. *Genome Biol*, 11(12),  
663 R123. <https://doi.org/10.1186/gb-2010-11-12-r123>
- 664 Li, S., Yamada, M., Han, X., Ohler, U., & Benfey, P. N. (2016). High-Resolution Expression Map of the  
665 *Arabidopsis* Root Reveals Alternative Splicing and lincRNA Regulation. *Developmental Cell*,  
666 39(4), 508–522. <https://doi.org/10.1016/j.devcel.2016.10.012>
- 667 Long, Y., Smet, W., Cruz-Ramírez, A., Castelijns, B., de Jonge, W., Mähönen, A. P., Bouchet, B. P.,  
668 Perez, G. S., Akhmanova, A., Scheres, B., & Blilou, I. (2015). *Arabidopsis* BIRD Zinc Finger  
669 Proteins Jointly Stabilize Tissue Boundaries by Confining the Cell Fate Regulator SHORT-ROOT  
670 and Contributing to Fate Specification. *The Plant Cell*, 27(4), 1185–1199.  
671 <https://doi.org/10.1105/tpc.114.132407>
- 672 Long, Y., Stahl, Y., Weidtkamp-Peters, S., Postma, M., Zhou, W., Goedhart, J., Sánchez-Pérez, M.-I.,  
673 Gadella, T. W. J., Simon, R., Scheres, B., & Blilou, I. (2017). In vivo FRET–FLIM reveals cell-type-  
674 specific protein interactions in *Arabidopsis* roots. *Nature*, 548, 97.  
675 <https://doi.org/10.1038/nature23317>
- 676 Nakajima, K., Sena, G., Nawy, T., & Benfey, P. N. (2001). Intercellular movement of the putative  
677 transcription factor SHR in root patterning. *Nature*, 413(6853), 307–311.  
678 <https://doi.org/10.1038/35095061>

- 679 Petricka, J. J., Winter, C. M., & Benfey, P. N. (2012). Control of *Arabidopsis* Root Development.  
680 *Annual Review of Plant Biology*, 63(1), 563–590. <https://doi.org/10.1146/annurev-arplant-042811-105501>
- 682 Pi, L., Aichinger, E., van der Graaff, E., Llavata-Peris, C. I., Weijers, D., Hennig, L., Groot, E., & Laux, T.  
683 (2015). Organizer-Derived WOX5 Signal Maintains Root Columella Stem Cells through  
684 Chromatin-Mediated Repression of CDF4 Expression. *Developmental Cell*, 33(5), 576–588.  
685 <https://doi.org/https://doi.org/10.1016/j.devcel.2015.04.024>
- 686 Prusinkiewicz, P., Crawford, S., Smith, R. S., Ljung, K., Bennett, T., Ongaro, V., & Leyser, O. (2009).  
687 Control of bud activation by an auxin transport switch. *Proceedings of the National Academy of  
688 Sciences of the United States of America*, 106(41), 17431–17436.  
689 <https://doi.org/10.1073/pnas.0906696106>
- 690 Radny, J., & Meyer, K. M. (2018). The role of biotic factors during plant establishment in novel  
691 communities assessed with an agent-based simulation model. *PeerJ*, 6, e5342.  
692 <https://doi.org/10.7717/peerj.5342>
- 693 Saltelli, A., Annoni, P., Azzini, I., Campolongo, F., Ratto, M., & Tarantola, S. (2010). Variance based  
694 sensitivity analysis of model output. Design and estimator for the total sensitivity index.  
695 *Computer Physics Communications*, 181(2), 259–270.  
696 <https://doi.org/https://doi.org/10.1016/j.cpc.2009.09.018>
- 697 Sarkar, A. K., Luijten, M., Miyashima, S., Lenhard, M., Hashimoto, T., Nakajima, K., Scheres, B.,  
698 Heidstra, R., & Laux, T. (2007). Conserved factors regulate signalling in *Arabidopsis thaliana*  
699 shoot and root stem cell organizers. *Nature*, 446(7137), 811–814.  
700 <https://doi.org/10.1038/nature05703>
- 701 Shannon, P., Markiel, A., Ozier, O., Baliga, N. S., Wang, J. T., Ramage, D., Amin, N., Schwikowski, B., &  
702 Ideker, T. (2003). Cytoscape: a software environment for integrated models of biomolecular  
703 interaction networks. *Genome Research*, 13(11), 2498–2504.  
704 <https://doi.org/10.1101/gr.1239303>
- 705 Sobol', I. M. (2001). Global sensitivity indices for nonlinear mathematical models and their Monte  
706 Carlo estimates. *Mathematics and Computers in Simulation*, 55(1), 271–280.  
707 [https://doi.org/https://doi.org/10.1016/S0378-4754\(00\)00270-6](https://doi.org/https://doi.org/10.1016/S0378-4754(00)00270-6)
- 708 Sozzani, R., Cui, H., Moreno-Risueno, M. A., Busch, W., Van Norman, J. M., Vernoux, T., Brady, S. M.,  
709 Dewitte, W., Murray, J. A. H., & Benfey, P. N. (2010). Spatiotemporal regulation of cell-cycle  
710 genes by SHORTROOT links patterning and growth. *Nature*, 466(7302), 128–132.  
711 <https://doi.org/10.1038/nature09143>
- 712 Spurrey, R. J., Van den Broeck, L., Clark, N. M., Fisher, A. P., de Luis Balaguer, M. A., & Sozzani, R.  
713 (2020). tuxnet: a simple interface to process RNA sequencing data and infer gene regulatory  
714 networks. *The Plant Journal : For Cell and Molecular Biology*, 101(3), 716–730.  
715 <https://doi.org/10.1111/tpj.14558>
- 716 Stahl, Y., Grabowski, S., Bleckmann, A., Kühnemuth, R., Weidtkamp-Peters, S., Pinto, K. G., Kirschner,  
717 G. K., Schmid, J. B., Wink, R. H., & Hülsewede, A. (2013). Moderation of *Arabidopsis* root  
718 stemness by CLAVATA1 and ARABIDOPSIS CRINKLY4 receptor kinase complexes. *Current  
719 Biology*, 23(5), 362–371.
- 720 The MathWorks, I. (2019). *SimBiology*. <https://nl.mathworks.com/products/simbiology.html>
- 721 van den Berg, C., Willemsen, V., Hendriks, G., Weisbeek, P., & Scheres, B. (1997). Short-range control  
722 of cell differentiation in the *Arabidopsis* root meristem. *Nature*, 390(6657), 287–289.  
723 <https://doi.org/10.1038/36856>
- 724 Van den Broeck, L., Gordon, M., Inzé, D., Williams, C., & Sozzani, R. (2020). Gene Regulatory Network

- 725        Inference: Connecting Plant Biology and Mathematical Modeling. *Frontiers in Genetics*, 11, 457.  
726        <https://doi.org/10.3389/fgene.2020.00457>
- 727        Vercruyssen, L., Verkest, A., Gonzalez, N., Heyndrickx, K. S., Eeckhout, D., Han, S.-K., Jégu, T.,  
728        Archacki, R., Van Leene, J., Andriankaja, M., De Bodt, S., Abeel, T., Coppens, F., Dhondt, S., De  
729        Milde, L., Vermeersch, M., Maleux, K., Gevaert, K., Jerzmanowski, A., ... Inzé, D. (2014).  
730        ANGUSTIFOLIA3 binds to SWI/SNF chromatin remodeling complexes to regulate transcription  
731        during *Arabidopsis* leaf development. *The Plant Cell*, 26(1), 210–229.  
732        <https://doi.org/10.1105/tpc.113.115907>
- 733        Yao, C.-W., Hsu, B.-D., & Chen, B.-S. (2011). Constructing gene regulatory networks for long term  
734        photosynthetic light acclimation in *Arabidopsis thaliana*. *BMC Bioinformatics*, 12(1), 335.  
735        <https://doi.org/10.1186/1471-2105-12-335>
- 736        Zhang, X., Zhou, W., Chen, Q., Fang, M., Zheng, S., Scheres, B., & Li, C. (2018). Mediator subunit  
737        MED31 is required for radial patterning of &lt;em&gt;*Arabidopsis*&lt;/em&gt; roots.  
738        *Proceedings of the National Academy of Sciences*, 115(24), E5624 LP-E5633.  
739        <https://doi.org/10.1073/pnas.1800592115>
- 740